

BOOK OF TUTORIALS AND ABSTRACTS



European Microbeam Analysis Society

EMAS 2009

11th

EUROPEAN WORKSHOP

on

MODERN DEVELOPMENTS

AND

APPLICATIONS

IN

MICROBEAM ANALYSIS

10 to 14 May 2009

at the

Hotel Spa Faltom

Gdynia/Rumia, Gdansk, Poland

Organized in collaboration with
Silesian University of Technology
Polish Society for Microscopy (PTMi)
Polish Academy of Sciences:
Committee of Materials Science, Institute of Physics,
Institute of Materials Science and Metallurgy



3-DIMENSIONAL ORIENTATION MICROSCOPY USING FIB-EBSD TOMOGRAPHY: AN OVERVIEW ON TECHNIQUES, APPLICATIONS, AND LIMITS

Stephan Zaefferer

Max-Planck-Institute for Iron Research, Diffraction and Microscopy Group
Max-Planck Strasse 1, DE-40237 Düsseldorf, Germany

Dr. Stefan Zaefferer studied Physical Metallurgy at the Technical University of Clausthal Zellerfeld. At the same place he pursued his Ph.D. studies in the Institute for Physical Metallurgy and Metal Physics, headed by Prof. H.-J. Bunge. During his Ph.D. studies – supervised by Prof. R. Schwarzer – he extensively used crystallographic analysis in TEM to investigate the deformation mechanisms and their relationship to the deformation texture in different titanium alloys. During that time he also wrote computer programmes for EBSD- and TEM-based orientation microscopy. He obtained his Ph.D. in 1995.

Following his Ph.D. he went for 2.5 years as a post-doc to the University of Paris-Sud in Orsay in the laboratory of Prof. Richard Penelle where he studied recrystallisation mechanisms in FeNi alloys, again extensively using TEM and developing computer programmes for TEM.

Subsequently he added a second post-doc stay at the Kyoto University in the laboratory of Prof. Tadashi Maki. After 2 years he left Japan and became in 2000 leader of the group for microscopy and diffraction at the Max-Planck Institute for Iron Research, Düsseldorf. His main interests are the physical mechanisms responsible for the formation of microstructures in metallic and intermetallic materials. Furthermore, he constantly develops microscopical and diffraction-based tools for his investigations. His group consists of about 8 to 10 scientific co-workers.

1. ABSTRACT

3-dimensional microstructure analysis techniques are essential for research on a number of problems in materials science. A powerful technique for 3D observations is FIB-EBSD tomography which is a combination of serial sectioning using a focussed ion beam (FIB) and observation of the sections by electron backscatter diffraction (EBSD) based orientation microscopy. The technique allows reaching at best a 3D resolution of $50 \times 50 \times 50 \text{ nm}^3$ where it yields information about crystal structure, orientation and defect density for every 3D element. At maximum a volume of about $100 \times 100 \times 100 \text{ }\mu\text{m}^3$ can be observed. Usual measurement times are in the order of 10 to 30 minutes per serial section, resulting in total measurement time of about 2 days for usual volumes. The technique enables accurate and quantitative observations on many crystalline materials. Nevertheless, for some materials (e.g., some intermetallics and minerals, metastable austenite in steels) the crystal structure is destroyed by the ion beam. They are therefore not accessible with this technique.

2. INTRODUCTION

2.1. The need for 3D observations

Conventional electron backscatter diffraction (EBSD) based orientation microscopy is a 2-dimensional (2D) characterisation method which is applied to plane cuts through a sample. Statistical stereological techniques [1-3], or <http://www.liv.ac.uk/fetoxpath/quantoxpath/stereol.htm>, or simply the observation of a given microstructure from different directions can be used to gain insight into the 3-dimensional (3D) aspects of the microstructure. However, there are also cases where a true 3-dimensional characterisation of a sample volume is critical to a correct understanding of the role the microstructure plays in a specific material behaviour or property. Examples for this are the deformation or recrystallisation behaviour, the progress of phase transformation, or the evolution of damage. In all these cases it is particularly beneficial if the 3D observation is performed in a non-destructive manner, such that the evolution of microstructure can be followed. Examples for appropriate techniques are the synchrotron radiation-based methods [4-8], and possibly also transmission electron microscopy-based methods [9].

In case of destructive 3D observation techniques, as the one we are reporting on here, critical applications are less frequent. One particular information that is obtained by 3D techniques is the full crystallographic characterisation of interfaces, e.g., grain boundaries. As displayed in Fig. 1, grain boundaries are defined by 5 macroscopic parameters, represented by the misorientation across the boundary (3 parameters) and its plane normal (2 parameters). In 2D orientation microscopy only the misorientation and the trace of the boundary can be determined, e.g., only 4 parameters are accessible.

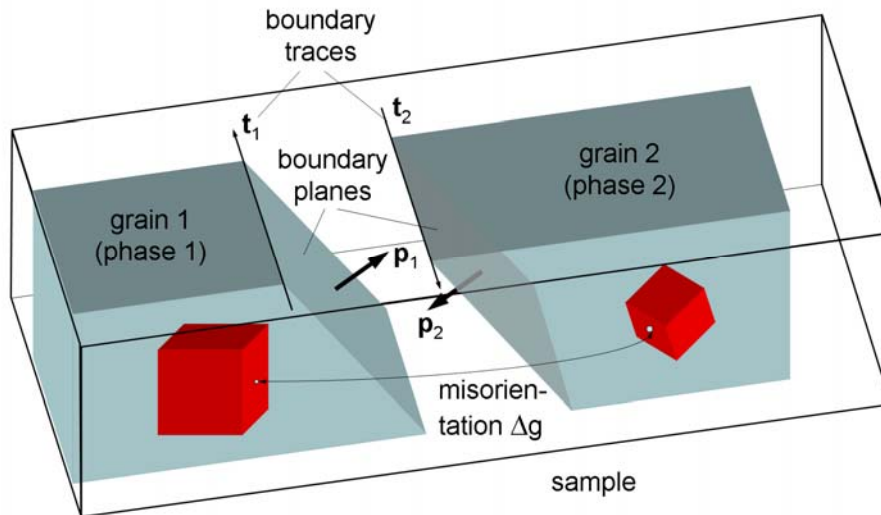


Figure 1. Schematic display of the 5 grain boundary parameters, $\Delta\mathbf{g}$ and \mathbf{p} . The trace vectors, \mathbf{t} , can be determined if only 2D measurements are available.

A second case where static 3D data are of importance is the physical modelling of microstructure formation processes (e.g., deformation or recrystallisation processes). In the past, microstructure modelling was frequently based on artificially created microstructures, assuming distributions of texture or grain morphology [10]. Realistic 3-dimensional input data may greatly enhance the significance of such models [11, 12].

Further examples where 3D information is essential include, for example, research on the connectivity of phases or boundaries (e.g., stress corrosion cracking of $\Sigma 3$ boundaries [13], the determination of dislocation densities from 3D crystal lattice rotation fields using the Nye-tensor approach [14], or the proof of hypotheses on models of grain growth which result in well-defined grain size distributions [15]).

2.2. Techniques for 3D observation

In principle, 3D-characterisation of microstructures can be performed by 2 different approaches, either by serial sectioning (destructive) or, in a non-destructive manner, by observation with some sort of transmissive radiation, e.g., synchrotron radiation. We report here on the serial sectioning approach. Sectioning techniques simply comprise the removal of slices of material with some cutting technique followed by the recording of the structure of the so-exposed materials surface with an appropriate microscopic technique. Finally the 3D structure is reconstructed, e.g., by stacking of the recorded images. Serial sectioning techniques are applicable to a wide range of materials and material problems with the only serious disadvantage that they are destructive.

A particularly well suited technique for 3D sectioning is the combination of serial sectioning with a focussed ion beam and EBSD-based orientation microscopy in a combined FIB (focussed ion beam) SEM. The sectioning with the ion beam allows creation of parallel and equally spaced sections, EBSD enables quantitative image interpretation, necessary for 3D reconstruction. For an overview on 3D serial sectioning techniques see the recent viewpoint set in Scripta Materialia [16-18]. Fully automated 3D orientation microscopy systems combining FIB and EBSD have been developed in the last few years by Mulders and Day [19] and Zaefferer et al. [20]. An overview on the technique and on investigations that have been done with it to date was recently published by Zaefferer et al. [21].

3. THE GEOMETRICAL SET-UP FOR 3D CHARACTERISATION IN A FIB SEM

A typical instrument for FIB-EBSD tomography consists of an SEM with a FIB mounted to its side at an angle of usually 54° from the vertical. The EBSD detector may be mounted either below the FIB column or on the opposite side of it. Both set-ups are sketched in Fig. 2. For EBSD the investigated surface is usually tilted 70° from the horizontal position while grazing incidence ion milling of the surface requires the surface to be inclined to 36° ($= 90^\circ - 54^\circ$). In the case that the EBSD detector is mounted to the opposite side of the FIB column the sample has to be tilted about an axis perpendicular to the electron and ion beam in order to change between the EBSD and the milling position. This set-up, displayed in Fig. 2a, is therefore called the “tilt”-set-up [12, 20]. In the other case the sample has to be rotated about an axis positioned at the half angle between the electron and ion beam (Fig. 2c). This set-up is called the “rotation” set-up [19]. A third set-up – which has, to the authors knowledge, not been used yet for 3D serial sectioning but probably offers the most powerful arrangement for 3D EBSD – is sketched in Fig. 2b: here the EBSD detector is mounted at 90° to both, the electron beam and ion beam direction. If the sample is positioned appropriately no sample movement between the milling and EBSD position is necessary at all. This set-up is therefore called the “static” set-up.

The accuracy and advantages and disadvantages of the different set-ups are discussed in more detail in Zaefferer and Wright [22].

4. AUTOMATIC 3D ORIENTATION MICROSCOPY

Automatic serial sectioning and EBSD mapping requires the synchronisation of SEM, FIB and the camera control hardware. All participating processes are controlled by one computer programme. Once the software is configured, it runs the milling and EBSD cycle until a predefined number of cycles has been reached.

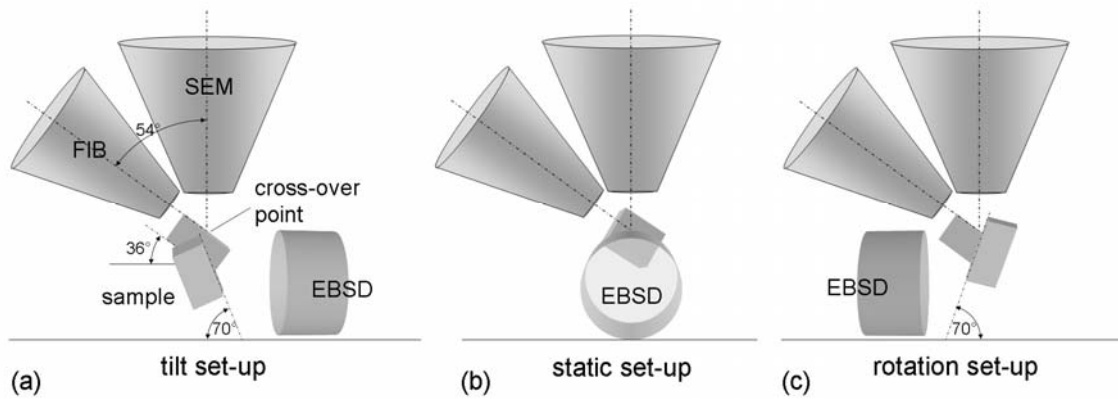


Figure 2. Schematics of the different geometrical set-ups of the EBSD-FIB tomography.
 (a) The tilt geometry – the sample has to be tilted to change between the milling and the EBSD position.
 (b) the static set-up – the sample does not have to be moved at all.
 (c) the rotation set-up – the sample is rotated to change between the positions.

Automatic 3D orientation microscopy puts high demands on the measurement process: (1) the stage positioning has to be accurate enough to allow redetection of the marker in each position in the limits of the beam shift controls. (2) The precision of stage tilt must be high enough to avoid any visible distortion of the field of view. (3) Stage drift after sample repositioning must be minimized and the stage must reliably come to a complete stop in the range of tens of seconds. (4) The position correction algorithm must be precise enough to achieve the desired resolution. (5) The SEM and the FIB must work stably over long measurement times.

4.1. Accuracy and application limits

Two important parameters to assess the performance of the technique are (i) the spatial resolution, and (ii) the maximum size of the observable volumes with regard to the long-term stability of the instrument. For a detailed discussion on these parameters see Zaefferer *et al.* [21].

(i) The spatial resolution of the system results from the *lateral* resolution achieved on the 2D sections, the accuracy of alignment of the sections and the *depth* resolution. Considering the accuracy of detection of the fiducial marker and the accuracy of sample tilt one finds that a depth resolution of 50 nm represents the best resolution currently achievable. Most of the studies performed so far have been carried out with 100 nm step sizes in all directions which gives satisfactory section alignment.

(ii) The maximum size of the observable volume depends mainly on the material and on the time investment one wants to make. Fig. 3 displays the typical appearance of an investigated area and defines the dimensions of it. While the width of the milled surface is virtually unlimited, the height of the observable surface depends on the sensitivity of the sample

material to curtaining. To date, the largest curtain-free height obtained by the author is larger than 100 μm on a FeNi sample milled with 500 pA beam current. Other authors [23] reached a smooth milling area height of almost 100 μm on a Ni-base superalloy.

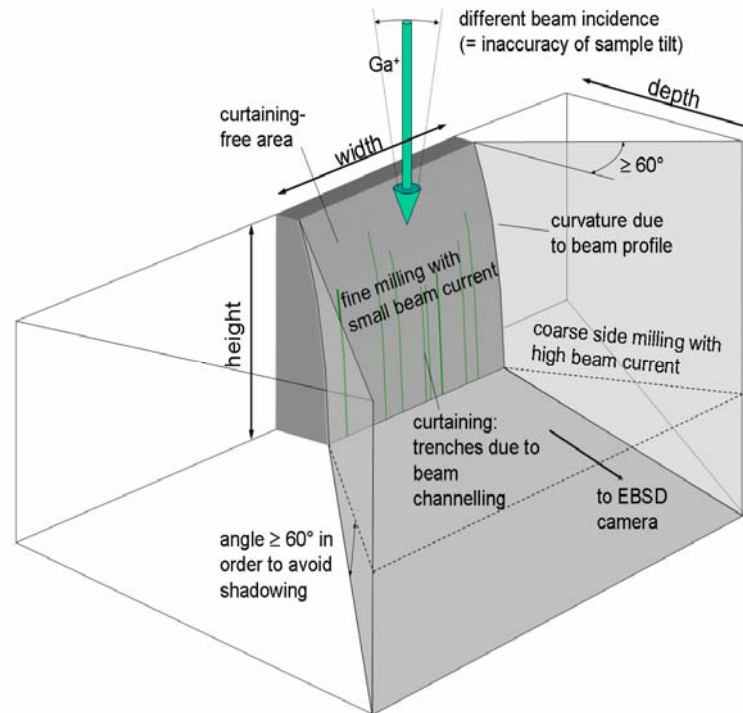


Figure 3. Schematic drawing of the milled area indicating some geometrical features and potential sources of inaccuracy.

The number and maximum thickness of milled sections is, as the width, in principle unlimited. However, with increasing milling depth the milled volume has to be increased in order to prevent shadows on the EBSD screen and serious re-deposition of milled material on the sides of the milled volume. Taking into account that a curtain-free area of $20 \times 20 \mu\text{m}$ (width \times height) may be milled 1 μm into a low-alloy steel sample in approximately 15 min with a beam current of 500 pA it can be estimated that the largest volume accessible with the method presented here is in the order of $w \times h \times d = 100 \times 100 \times 100 \mu\text{m}^3$ (if using special sample geometries, see e.g., Groeber *et al.* [18]).

4.2. Materials issues

On many materials the surfaces created by FIB milling show sufficiently low radiation damage to preserve the crystal structure close to the surface [24-26]. Therefore, on many metals and intermetallics investigated so far (various ferritic, austenitic and martensitic steels, nickel, copper, aluminium, FeAl, CuZnAl) excellent diffraction patterns were obtained from milled

surfaces and the microstructures observed on these were similar to those prepared by other methods. Nevertheless, various problems exist. One is the amorphisation of certain materials. We have observed, for example, that Nb-containing Laves-phase precipitates in Fe₃Al, which give clear diffraction patterns after mechanical preparation, do not give any patterns when prepared by milling [27]. A second, serious problem has been observed when milling steels with metastable residual austenite, for example low-alloyed TRIP steels. Here, all austenite transforms under influence of the ion beam into ferrite. Up to now, this transformation could not be avoided by either small beam currents or by low-kV milling or a milling with Ar⁺ ions. Finally, we observed that the microstructure of heavily deformed aluminium may be destroyed by intense ion beam irradiation which can probably be attributed to the formation of a low-temperature melting Al-Ga eutectic.

5. APPLICATION EXAMPLES

The 2 examples described in the following have been collected in the author's lab on a Zeiss Crossbeam XB 1540 FIB-SEM which consists of a Gemini-type field emission gun electron column and an Orsay Physics ion beam column. For EBSD, a DigiView camera of Edax-TSL was mounted opposite to the FIB column on a motorised and computer-controlled slide. The geometric arrangement is a tilt set-up as described earlier. The SEM was operated at an acceleration voltage of 15 kV, the FIB at 30 kV. The cross-over point of the system is at 8 mm, the optimum EBSD working distance at 12 mm.

5.1. Microstructure of "nanocrystalline" NiCo deposits

Electrodeposition from aqueous solution has been intensively studied as a method to create metallic films with nanocrystalline microstructure [28-31]. The deposition parameters, such as solution composition, current density and bath movement strongly influence the developing microstructure. The exact mechanisms of microstructure formation are still largely unknown, also because a precise characterisation of the microstructure has rarely been undertaken. In a recently published work [32] we applied EBSD-based high resolution orientation mapping to obtain a deeper knowledge on the microstructure of electrodeposited thin films of NiCo. Most of the investigated films consist to a large volume fraction of columnar crystals with cross-sections in the sub-micrometre range but lengths in the order of more than 30 μm as shown in Fig. 4a. For all columnar grains the $\langle 1\ 1\ \bar{2}\ 0 \rangle$ direction is close to the growth direction of the crystal column. Only in niches beside these crystals do areas of truly nanocrystalline material exist. It was furthermore found that the elongated crystals are in most cases growing in triples of 3 parallel crystals which are related to each other by a twin orientation relationship. The existence of these triples can be seen on the free grown surface of the electrodeposited material in the form of 3-fold pyramids as shown in Fig. 4b. We suspect that the existence of twins stabilizes the growth of columnar grains by formation of low energy boundaries.

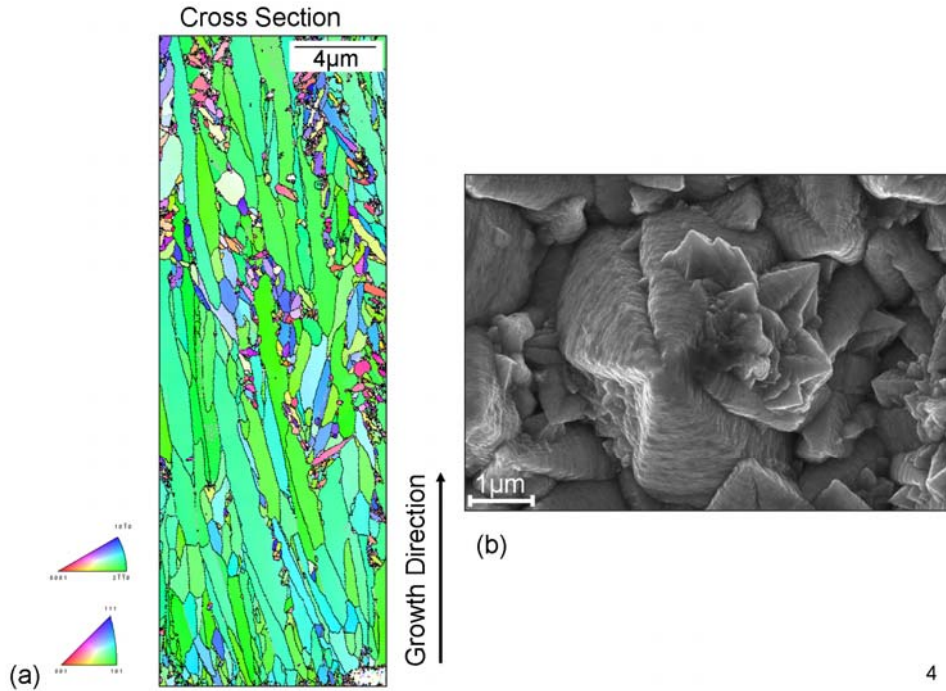


Figure 4. (a) Cross-section orientation map of the microstructure of columnar-grown NiCo electrodeposited film. (b) Surface morphology of the film, showing the formation of 3-fold pyramids.

3D orientation microscopy was performed on a full, 100 μm wide cross-section of an electrodeposited material. The sample was manually ground and polished on the cross-sections to produce a sharp rectangular edge as shown in Fig. 5. A step size of 100 nm in all dimensions was selected and 60 maps covering a volume of $83 \times 16 \times 6 \mu\text{m}^3$ were measured within less than 2 days. The results are shown in Fig. 6a as a 3D orientation map, coloured according to the inverse pole figure of a direction perpendicular to the growth direction. Random large angle grain boundaries are coloured black while all possible twin boundaries are displayed as white lines. In the centre of the map a part has been cut out to expose a typical twin-triple consisting of 3 grains with two $56^\circ \langle 1\ 1\ \bar{2}\ 0 \rangle$ twin relations between them and an approximately $66^\circ \langle 1\ 1\ \bar{2}\ 0 \rangle$ relationship on the remaining boundary. In Fig. 6b the block is cut along the plane that contains this twin triple. The triple is not growing straight but is visibly quite heavily curved. Together with this curvature the orientation of the triple changes as shown in by the colour code of the figure which displays the deviation of the macroscopic growth direction from the $\langle 1\ 1\ \bar{2}\ 0 \rangle$ crystal direction.

From Fig. 6b it is noticed that the grains (1) and (2) exist as twins with a sharp $57^\circ \langle 1\ 1\ \bar{2}\ 0 \rangle$ relation already when they first enter into the measurement area (marked as point A in Fig. 6b) (note that grain (2) is not visible in the figure as it is on top of grain (1)). At point B, grain (3) nucleates and grows for the first approximately 10 μm as a very thin tube parallel to grains (1) and (2). At the position where the grains reach a position for optimum growth (i.e. $\langle 1\ 1\ \bar{2}\ 0 \rangle$)

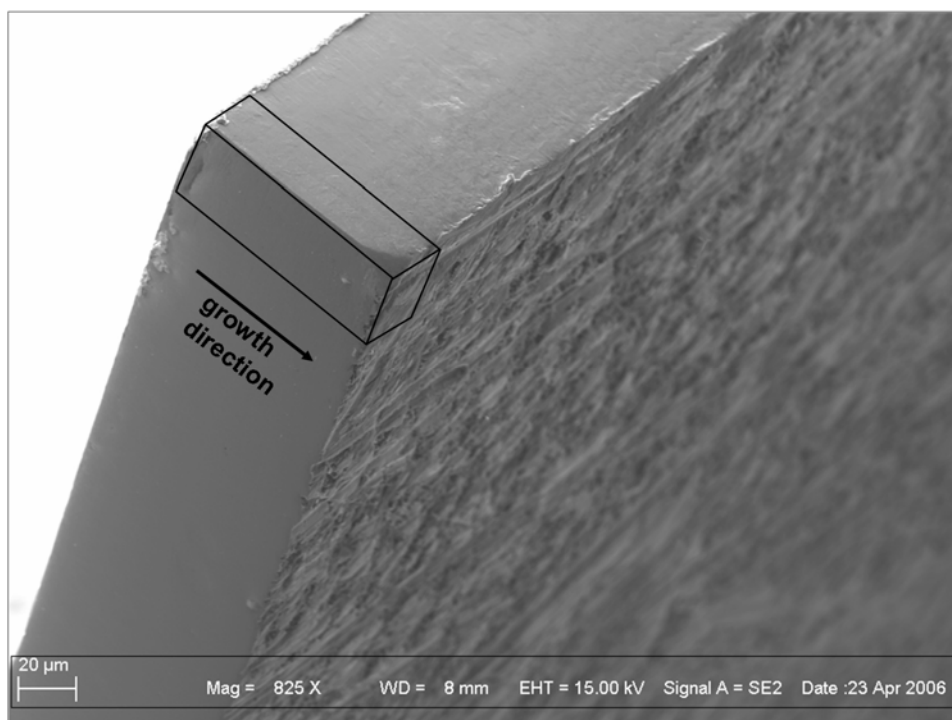


Figure 5. Secondary electron image of the cross-section of the NiCo thin film ready for 3D orientation microscopy. The investigated volume is indicated by a black line frame, the growth direction by an arrow. The rectangular edge has been prepared by mechanical grinding and polishing.

parallel to the macroscopic GD) grain (3) also expands and grows larger (point C). At this position the grain boundary characteristics were determined in more detail; the results are displayed in Fig. 6c. Between grain (1) and (2) a $\{1\ 0\ \bar{1}\ 1\}$ coherent twin boundary is found. Grain (3), although it shows a precise twin orientation relation with grain (2), does not have a coherent boundary with the latter, i.e., the plane indices on both sides of the grain boundary are different, the one of grain (2) being very precisely the $(0\ 0\ 0\ 1)$ basal plane, the other one being some quite highly indexed one. The same is true for the boundary with grain (1) although this grain boundary does not even show any typical twin orientation relationship. We conclude that the triple grain arrangement form low energy boundaries which support the growth of the triples (see Bastos *et al.* [33] for more information).

5.2. Modelling of nucleation of recrystallisation in Fe 36 % Ni

Fe 36 % Ni is a material with face centred cubic crystal structure and high stacking fault energy. During recrystallisation of cold rolled material it develops a sharp cube texture. The origin of the cube texture is oriented nucleation of cube-oriented grains in deformed cube-oriented bands. The reason for this preferred nucleation has long time been under

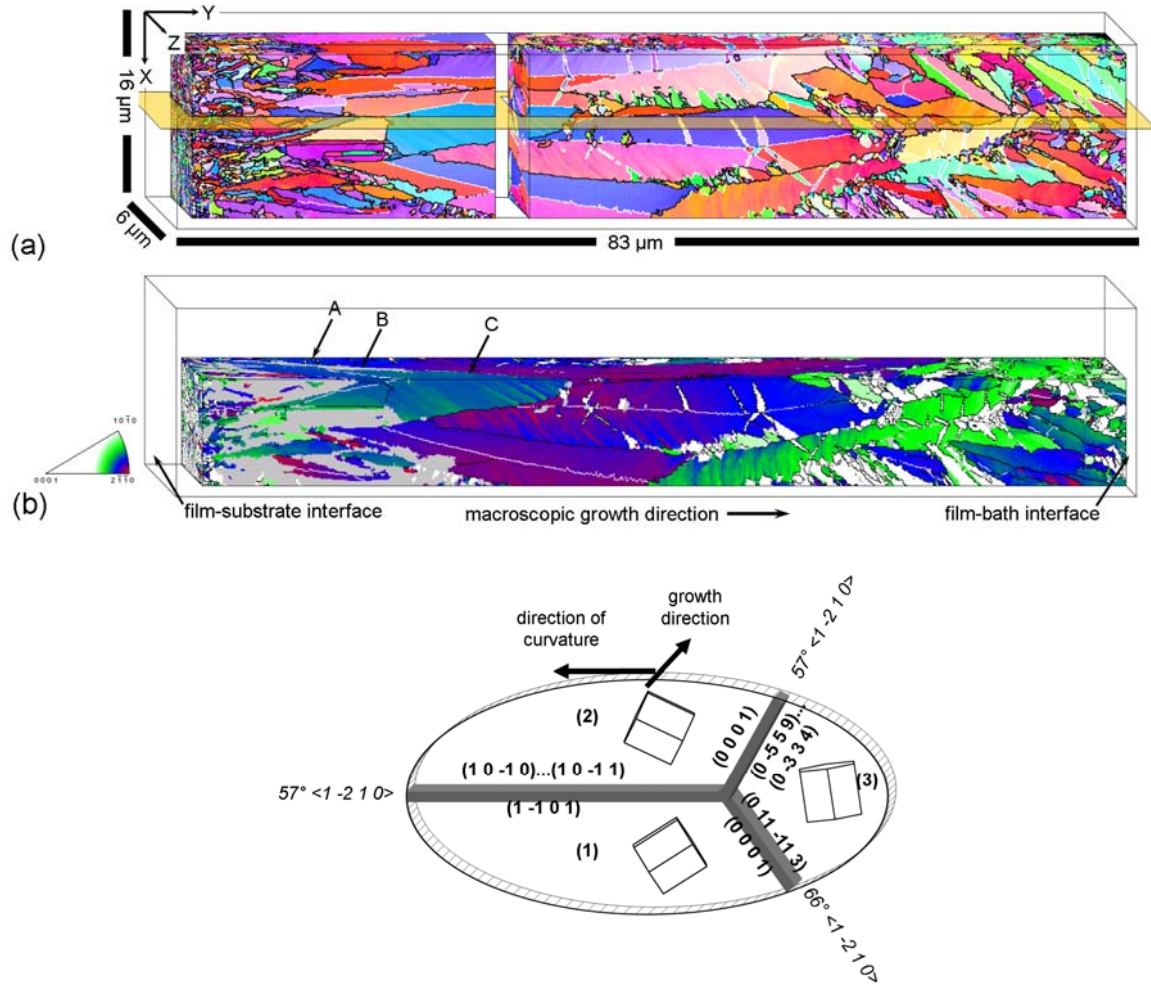


Figure 6. 3D orientation maps from a NiCo electrodeposited film. Measurement voxel size $100 \times 100 \times 100 \text{ nm}^3$.

(a) The full measured orientation map coloured according to the inverse pole figure of the X-direction. General large angle grain boundaries ($\theta > 15^\circ$) are displayed in black, all kind of twin boundaries in white. A part is cut-out in the middle to display the position of one twin-triple, marked by a circle.

(b) Orientation map coloured according to the deviation of the crystal $\langle 1\ 1\ \bar{2}\ 0 \rangle$ direction to the macroscopic growth direction Y. Areas in gray indicate crystals with fcc crystal structure. The structure is cut along the plane marked in (a).

(c) Grain boundary analysis on the twin-triple observed above. Crystals (1) and (2) form a coherent $57^\circ \langle 1\ 1\ \bar{2}\ 0 \rangle$ compression-type twin. Crystal (3) is in a non-coherent twin relation to crystal (2) but it has no special relationship with (1). Grains (2) and (3) and (1) and (3) have basal planes as boundary planes.

debate, also because the nucleation event cannot be observed directly. A promising way to surpass the problems of direct experimental observation of the nucleation event is the computer simulation of the process assuming reasonable physical models. On the microscopic scale of nucleation the Potts model solved by a Monte Carlo algorithm is an ideal method to perform

such simulations. Most frequently, the Potts model is applied to model normal grain growth [34], but it can also be applied to sub-grain growth processes, i.e., to nucleation [10, 35, 38] applied such a model to study the nucleation of cube grains in cold rolled Fe₃₆Ni alloys. As input data they used experimental orientation maps obtained by TEM which were combined with stored energy values from neutron diffraction measurements.

We recently applied a more refined Monte-Carlo technique to simulate the nucleation process in heavily cold rolled Fe₃₆%Ni. A computer programme for a 2D Potts model simulation originally developed for normal and abnormal grain growth by Chen *et al.* [37] was extended into 3D and adapted to the problem of normal sub-grain growth. As input data serve orientation maps obtained by 3D EBSD based orientation microscopy. In order to simulate sub-grain growth specific assumptions on grain boundary energy and mobility functions in dependence of the misorientation angle were made which are described in detail in Zaefferer [38]. The energy stored inside of sub-grains or grains is directly incorporated in the calculation as the low-angle grain boundary energy of boundaries between neighbouring points. This has the big advantage that no calibration of boundary versus volume energies is necessary.

The simulations were started on the basis of a 1-minute annealed structure which had already formed sub-grain structures displayed in Figs. 7a,b as left most figures (MSC = 0). It must be noted that the nucleation of cube grains was in this stage of annealing in principle already terminated as the cube grains had already a supercritical size and large angle grain boundaries. Thus only the early growth process was simulated. The other parts of Fig. 7 show microstructure snapshots obtained after different Monte Carlo steps (MCS). Fig. 7a displays the microstructure in terms of orientations while Fig. 7b shows the evolution of the so-called kernel average misorientation (KAM) maps which represent the residual stored energy in the microstructure.

One short conclusion drawn from these observations is that the cube-oriented grain keeps its low energy advantage over other grains during the whole growth process. This effect is responsible for the rapid growth of these grains. For a more detailed discussion of the subject see Zaefferer [38].

6. CONCLUSIONS

Automated 3D orientation microscopy yields a multidimensional data vector for each voxel of the measured volume, including the crystal orientation, the crystallographic phase, a value for the lattice defect density, and, if measured by simultaneous EDS analysis, the elemental composition. A volume pixel resolution of $100 \times 100 \times 100 \text{ nm}^3$ has been obtained as a standard but $50 \times 50 \times 50 \text{ nm}^3$ seems to be realistic optimum. Other authors have claimed an even better resolution of $20 \times 20 \times 20 \text{ nm}^3$ [19]. The largest volumes observable are in the

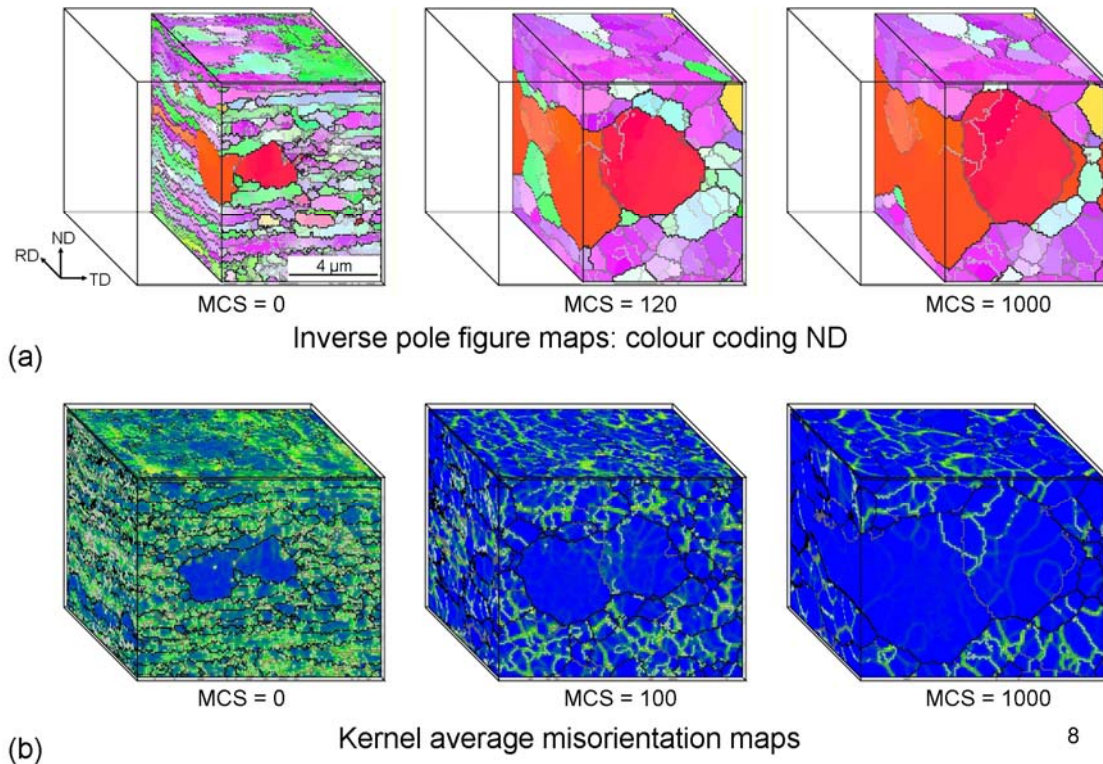


Figure 7. Measured 3D orientation maps (MSC = 0) and 2 stages of a 3D Monte Carlo simulation showing the progress of cube nucleus growth in a heavily cold rolled Fe 36 % Ni sample. The inverse pole figure maps show the crystal orientation (red: cube orientation $\{001\}\langle 100\rangle$), the kernel average misorientation maps display the stored energy. MCS: Monte Carlo steps.

order of $100 \times 100 \times 100 \mu\text{m}^3$. On particular materials (Ni-based superalloys) larger volumes have been reported. The technique works on a large number of materials but some exceptions have been found where the materials microstructure is significantly changed under Ga^+ -ion beam irradiation. The time per sectioning cycle currently develops in the direction of 10 to 30 minutes.

One main disadvantage of the FIB-EBSD tomography is the fact that it is a destructive technique, thus 3D observations of materials processes can not be performed. However, the combination with computer simulation tools offers the possibility to investigate also the evolution of microstructures. A second serious disadvantage is the relatively small volume that can be observed with the technique. Statistical data like grain size distributions or textures thus may be quite questionable and must be carefully checked. Here another powerful technique, the combination of EBSD with serial sections created by mechanical polishing (MP-EBSD tomography), allows a large extension of the observed volume. Unfortunately, this technique (MP-EBSD tomography) is extremely laborious and is, in fact, difficult to be fully automated. In comparison to the newly developed 3D X-ray diffraction techniques the strength of the FIB

EBSD-tomography technique lies in the significantly higher spatial resolution, applicability also to highly deformed or multi-phase structures, and ease of application.

7. REFERENCES

- [1] Adams B L (1986) *Met. Trans.* **17A**: 2199.
- [2] Adams B L, Morris P R, Wang T T, Willden K S and Wright S I (1987) *Acta Met.* **35**: 2935.
- [3] Howard C V and Reed M G (1998) Unbiased stereology - Three dimensional measurement in microscopy. Oxford, Bios Scientific Publ.
- [4] Poulsen H F *et al.* (2004) *J. Appl. Cryst.* **34**: 751.
- [5] Yang W *et al.* (2004) *Micron* **35**: 431.
- [6] Preusser A, Klein H and Bunge H J (2005) *Solid State Phenomena* **105**: 41334.
- [7] Lauridsen E M, Schmidt S, Nielsen S F, Margulies L, Poulsen H F and Juul-Jensen D (2006) *Scripta Mat.* **55**: 51-56.
- [8] Margulies L, Winther G and Poulsen H F (2001) *Science* **291**: 2392.
- [9] Midgley P A and Weyland M (2003) *Ultramicroscopy* **96**: 413-431.
- [10] Holm E A, Miodownik M A and Rollett A D (2003) *Acta Mater.* **51**: 2701-2716.
- [11] Zaaferani N, Raabe D, Singh R N, Roters F and Zaefferer S (2006) *Acta Mater.* **54**: 1863-1876.
- [12] Zaefferer S (2008) 3D EBSD-based orientation microscopy and 3D materials simulation tools: an ideal combination to study microstructure formation processes. in: EMC 2008, vol. 1: Instrumentation and methods (Luysberg M, Tillmann K and Weirich T, eds.). Berlin-Heidelberg, Springer Verlag, 641-642.
- [13] Rahimi S, Engelberg D L, Duff J A and Marrow T J (2009) *J. Microscopy* **233**: 423-431.
- [14] Demir E, Raabe D, Zaaferani N and Zaefferer S (2009) *Acta Mater.* **57**: 559-569.
- [15] Barrales Mora L A, Gottstein G and Shvindlerman L S (2008) *Acta Mater.* **56**: 5915-5926.
- [16] Spanos G (2006) *Scripta Mat.* **55**: 3.
- [17] Uchic M D, Groeber M, Wheeler R, Scheltens F and Dimiduk D M (2004) *Microsc. Microanal.* **10**: 1136-1137.
- [18] Groeber M A, Haley B K, Uchic M D, Dimiduk D M and Gosh S (2006) *Mat. Character.* **57**: 259-273.
- [19] Mulders J J L and Day A P (2005) *Mat. Sci. Forum* **495-497**: 237-242.
- [20] Zaefferer S, Konrad J and Raabe D (2005) 3D-orientation microscopy in a combined focused ion beam (FIB) - scanning electron microscope: a new dimension of microstructure characterisation. in: Microscopy Conference 2005, Davos, 63.
- [21] Zaefferer S, Wright S I and Raabe D (2008) *Met. Mater. Trans.* **39A**: 374-389.

- [22] Zaefferer S and Wright S I (2009) 3D-orientation microscopy by serial sectioning and EBSD-based orientation mapping in a FIB-SEM. in: EBSD in materials science, 2nd edition (Schwartz A et al., eds), in print.
- [23] West G (2007) private communication.
- [24] Prasad S V, Michael J R and Christenson T R (2003) *Scripta Mater.* **48**: 255-260.
- [25] Michael J R, Schischka J and Altmann F (2003) in: HKL Technology EBSD application catalogue. Hobro (Denmark), HKL Technology.
- [26] Matteson T L, Schwarz S W, Houge E C, Kempshall B W and Gianuzzi L A (2002) *J. Electronic Mater.* **31**: 33-39.
- [27] Konrad J, Zaefferer S and Raabe D (2006) *Acta Mater.* **54**: 1369-1380.
- [28] Vicenzo A and Cavallotti P L (2004) *Electrochim. Acta* **49**: 4079-4089.
- [29] Gómez E, Ramirez J and Vallés E (1998) *J. Appl. Electrochem.* **28**: 71-79.
- [30] El-Sherik A M and Erb U (1995) *J. Mater. Sci.* **30**: 5743-5749.
- [31] Wu B Y C, Ferreira P J and Schuh C A (2005) *Met. Mater. Trans. A* **36**: 1927-1936.
- [32] Bastos A, Zaefferer S, Raabe D and Schuh C (2006) *Acta Mater.* **54**: 2451-2462.
- [33] Bastos A, Zaefferer S and Raabe D (2008) *J. Microscopy* **230**: 487-498.
- [34] Rollett A D and Raabe D (2001) *Comp. Mat. Sci.* **21**: 69-78.
- [35] Baudin T, Julliard F, Paillard P and Penelle R (200) *Scripta Mater.* **43**: 63-68.
- [36] Baudin T, Solas D, Etter A L, Ceccaldi D and Penelle R (2004) *Scripta Mater.* **51**: 427-430.
- [37] Chen N, Zaefferer S, Lahn L, Günther K and Raabe R (2003) *Acta Mater.* **51**: 1755-1765.
- [38] Zaefferer S (2009) Orientation microscopy in SEM and TEM: fundamentals, techniques and applications in physical metallurgy. Habilitationsschrift, to be published.